Supplementary Information

Significant decrease in the ionization energy of dinaphtho[2,3-*b*:2′,3′-*f*]thieno[3,2-*b*]thiophene (DNTT) solid induced by a pinacolborane group

Kazuo Takimiya,[1,2,3]* Sayaka Usui,[2] Ryota Hanaki,[2] Kirill Bulgarevich,[1] Kohsuke Kawabata,[1,2] Kyohei Nakano,[1] Keisuke Tajima[1]

[1]RIKEN Center for Emergent Matter Science, 2-1 Hirosawa, Wako, Saitama 351-0198, Japan
[2]Department of Chemistry, Graduate School of Science, Tohoku University, 6-3 Aoba, Aramaki, Aoba-ku, Sendai 980-8578, Miyagi, Japan
[3]Tohoku University Advanced Institute for Materials Research (AIMR), 2-1-1 Katahira, Aoba-ku, Sendai 980-8577, Miyagi, Japan

Contents

1. Characterization of Bpin-DNTT

1.1 ^{1}H and ^{13}C NMR spectra

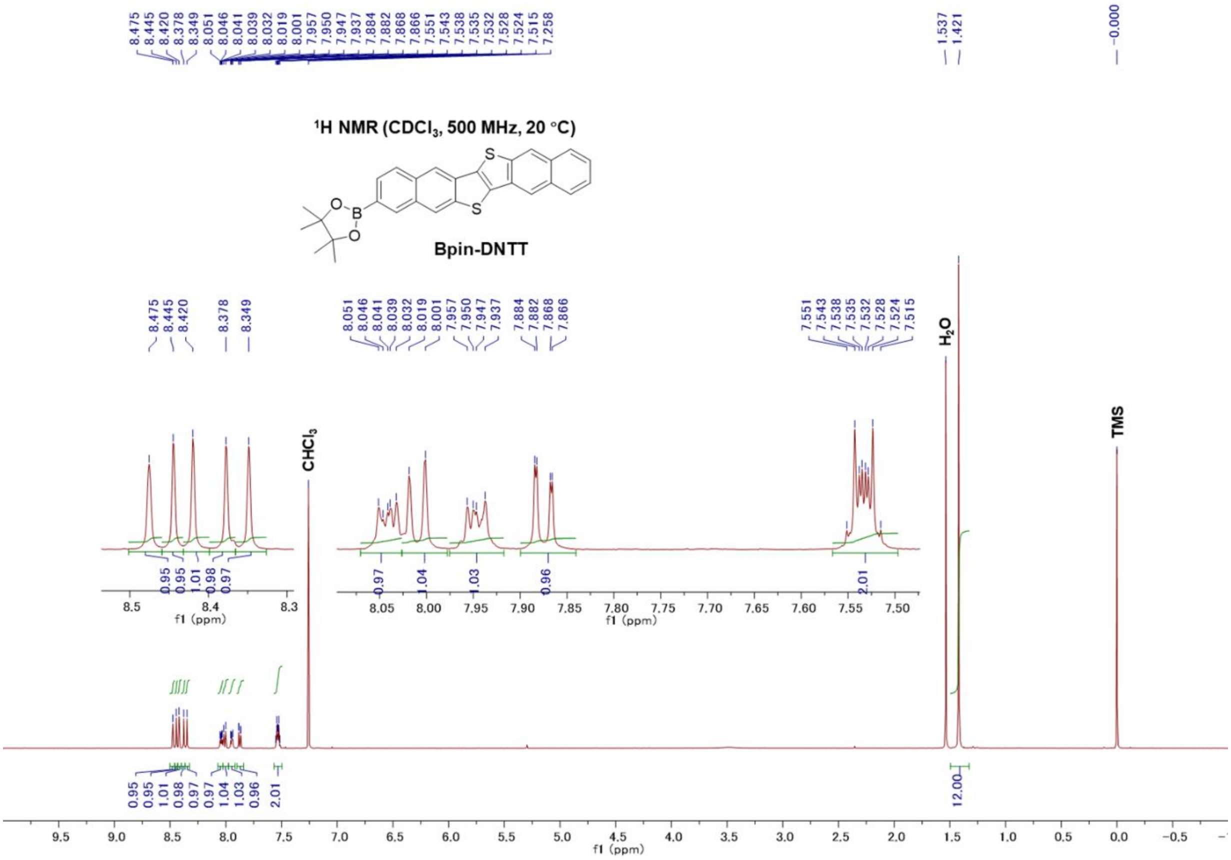

Fig. S1. ^{1}H NMR spectrum of Bpin-DNTT.

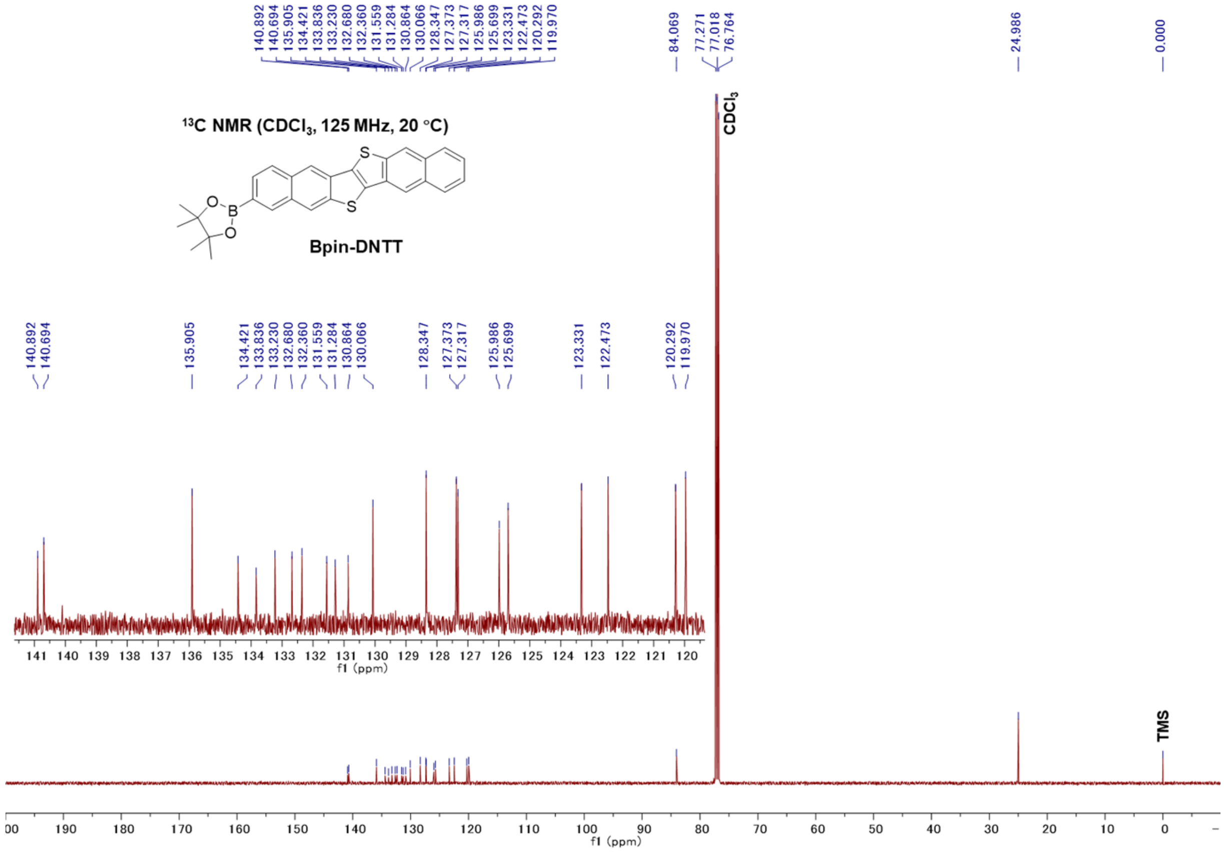

Fig. S2. ^{13}C NMR spectrum of Bpin-DNTT.

1.2 Evaluation of HOMO energy levels of Bpin-DNTT and DNTT

Electrochemistry: Cyclic voltammograms were recorded on an ALS Electrochemical Analyzer Model 612D with the three-electrode system consisting of a platinum disc working electrode ($\varphi = 3$ mm), a platinum wire counter electrode, and an Ag/AgCl reference electrode in a dichloromethane solution containing a substrate (0.05 mM) and tetrabutylammonium hexafluorophosphate (0.1 M) at a scan rate of 10 mV s^{-1}. All potentials were calibrated against the half-wave potential of the ferrocene/ferrocenium redox couple, measured under identical conditions.

Theoretical calculations: DFT calculations for structural optimization and estimation of energy levels of the frontier molecular orbitals were performed at the B3LYP/6-311G(d) level using the Gaussian 16 program package. [1]

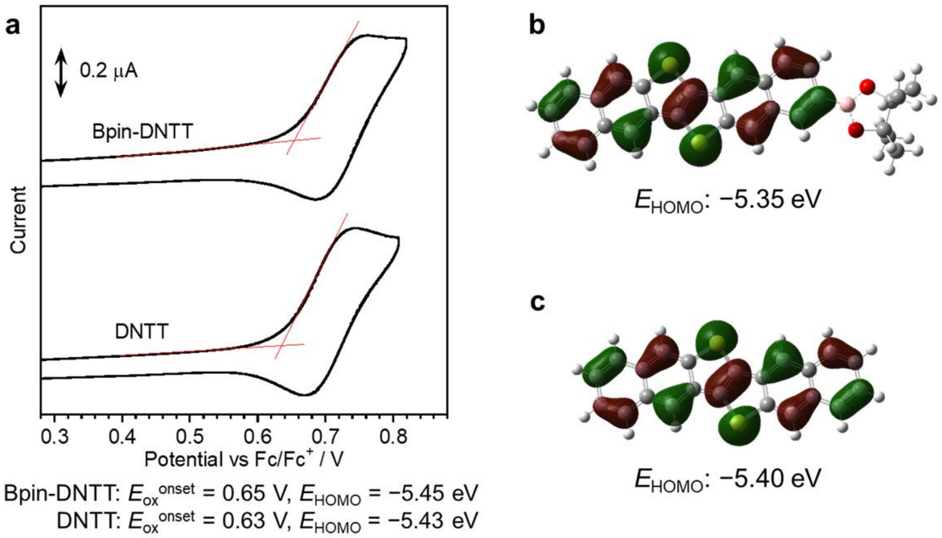

Fig. S3. Cyclic voltammograms of Bpin-DNTT (top) and DNTT (bottom) (a), and theoretically calculated HOMOs of Bpin-DNTT (b) and DNTT (c) at the level of B3LYP/6-311G(d) by Gaussian16.

2 Characterization of Bpin-DNTT thin-film

2.1 Fabrication and evaluation of Bpin-DNTT-based TFTs

2.1.1 Preparation of octadecylsilane- (ODTS-) and octylsilane- (OTS-) treated Si/SiO_2 substrates

Bottom-gate-top-contact TFT devices were fabricated on a heavily doped n^+-Si(100) wafer with a 200-nm-thick thermally grown SiO2 layer ($C_i = 17.3$ nF cm^{-2}). The Si/SiO_2 substrates (10 × 7 mm, S3) were ultrasonicated in water for 3 min thrice, followed by 10 min in acetone and isopropanol, respectively. They were then rinsed in boiling isopropanol for 10 min and subjected to UV-ozone treatment for 30 min. For ODTS-treated substrates, onto the cleaned substrate, a solution of octadecyltriethoxysilane in trichloroethylene (3 mM) was applied, and after 10 s the applied solution was spin-off at a spin-rate of 3000 rpm for 15 s, which was followed by hydrolysis in a closed container in the presence of ammonia hydroxide solution for 24 h. Then, the substrates were rinsed with water and boiling isopropanol. For octylsilane-treated substrates, the cleaned substrates were placed in a closed container in the presence of several drops of octyltrimethoxysilane and then kept in an oven at 80 °C overnight. The substrates were subsequently rinsed with boiling isopropanol.

2.1.2 Fabrication of TFT devices based on spin-coated thin films.

A solution of Bpin-DNTT (3 g L^{-1}) in chloroform (containing 1 vol% of toluene) was spin-coated on the OTS-treated Si/SiO_2 substrates at a spin rate of 3000 rpm for 15 sec. On top of the thin films, gold drain and source contact electrodes (thickness: 40 nm) with the channel length and width of 100 and 1500 µm, respectively, were vacuum-deposited through shadow masks under 10^{-4} Pa.

2.1.3 Evaluation of TFT devices

Current-voltage characteristics of the vacuum-deposited TFT devices were measured with a Keithley 4200-SCS semiconductor parameter analyzer in a nitrogen-filled glovebox just after fabrication, after two days of storage in the glovebox, and after exposure to the air for six days. Current-voltage characteristics of the spin-coated TFT devices were measured in air just after fabrication.

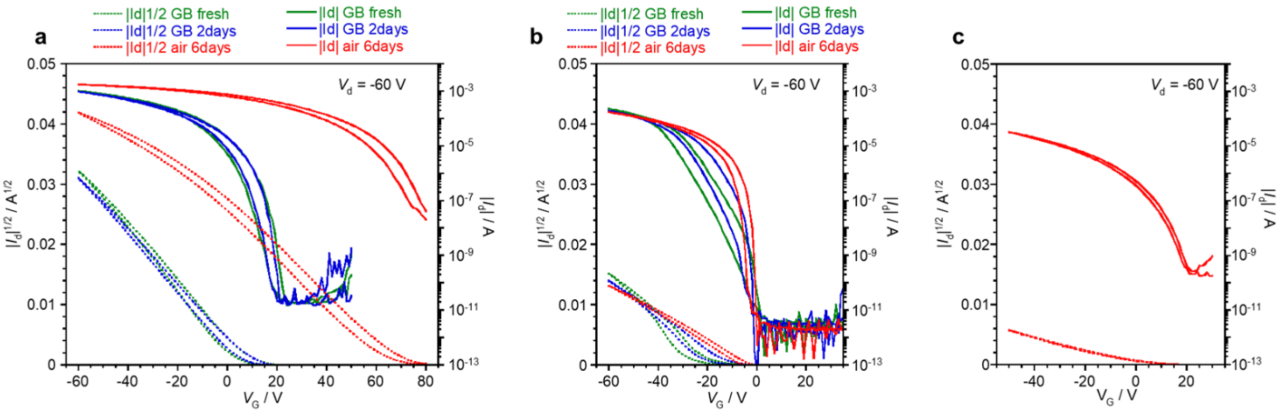

Fig. S4. Transfer characteristics of TFT devices based on vacuum-deposited Bpin-DNTT (a) and DNTT (b) thin films before and after exposure to the air and the TFT device based on spin-coated Bpin-DNTT thin film after exposure to air (c).

2.2 Thin-film XRD of vapor-deposited thin film of Bpin-DNTT

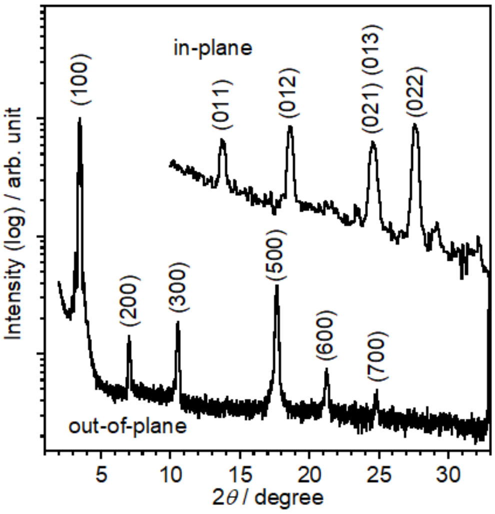

Fig. S5. Thin-film XRD patterns of Bpin-DNTT: in-plane (top) and out-of-plane (bottom) measurements.

2.3 Evaluation of Seebeck coefficient (*S*)

The sample was placed on two Peltier modules to apply the temperature-difference (ΔT) cycle (Fig. S6a). First, ΔT was kept at 0 K for 200 seconds, raised to 1 K (150 seconds), then to 2 K (150 seconds), and again set to 0 K. Then, another ΔT cycle with reversed temperature differences was applied (Fig. S6b). During these ΔT cycles, the thermovoltage (ΔV) was monitored every two seconds, and the ΔVs between 100 and 150 seconds in each step were averaged. The *S* was calculated from the slope of ΔV measured at the five different ΔTs (Fig. S6c).

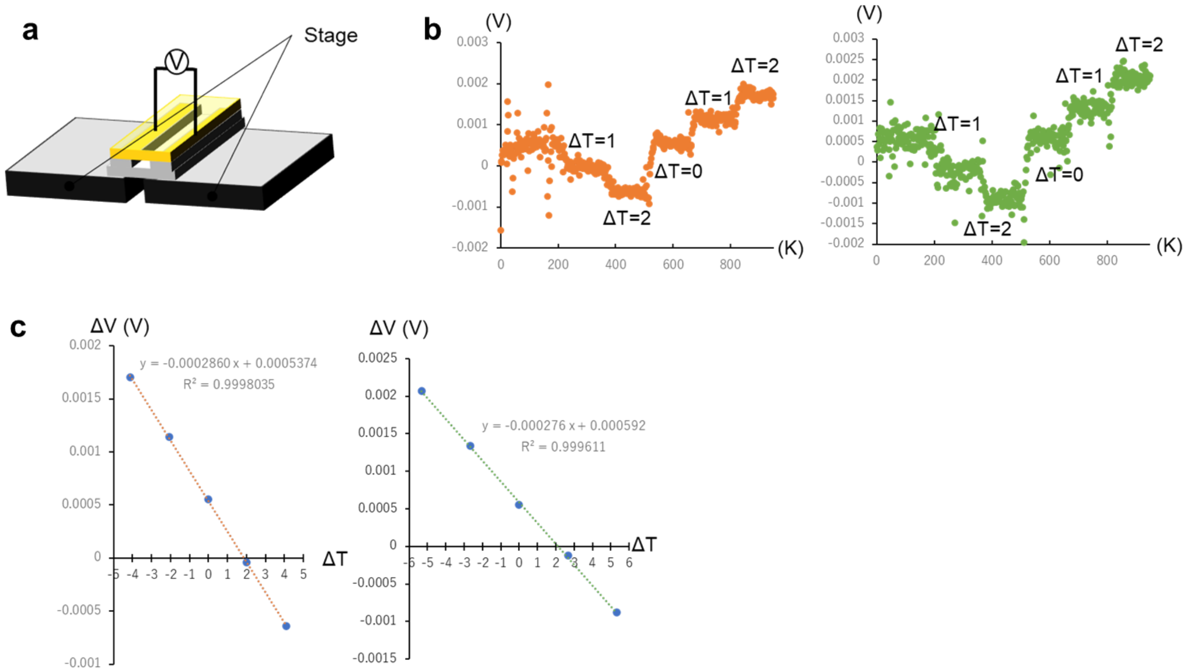

Fig. S6. Measurement of thermal electromotive force. (a) Schematic picture of the sample stage. (b) Two different samples were measured, and (c) the *S*s extracted from two different devices were 286 and 276 μV K^{-1}, respectively.

2.4 AFM images of vapor-deposited Bpin-DNTT and DBTT thin-films

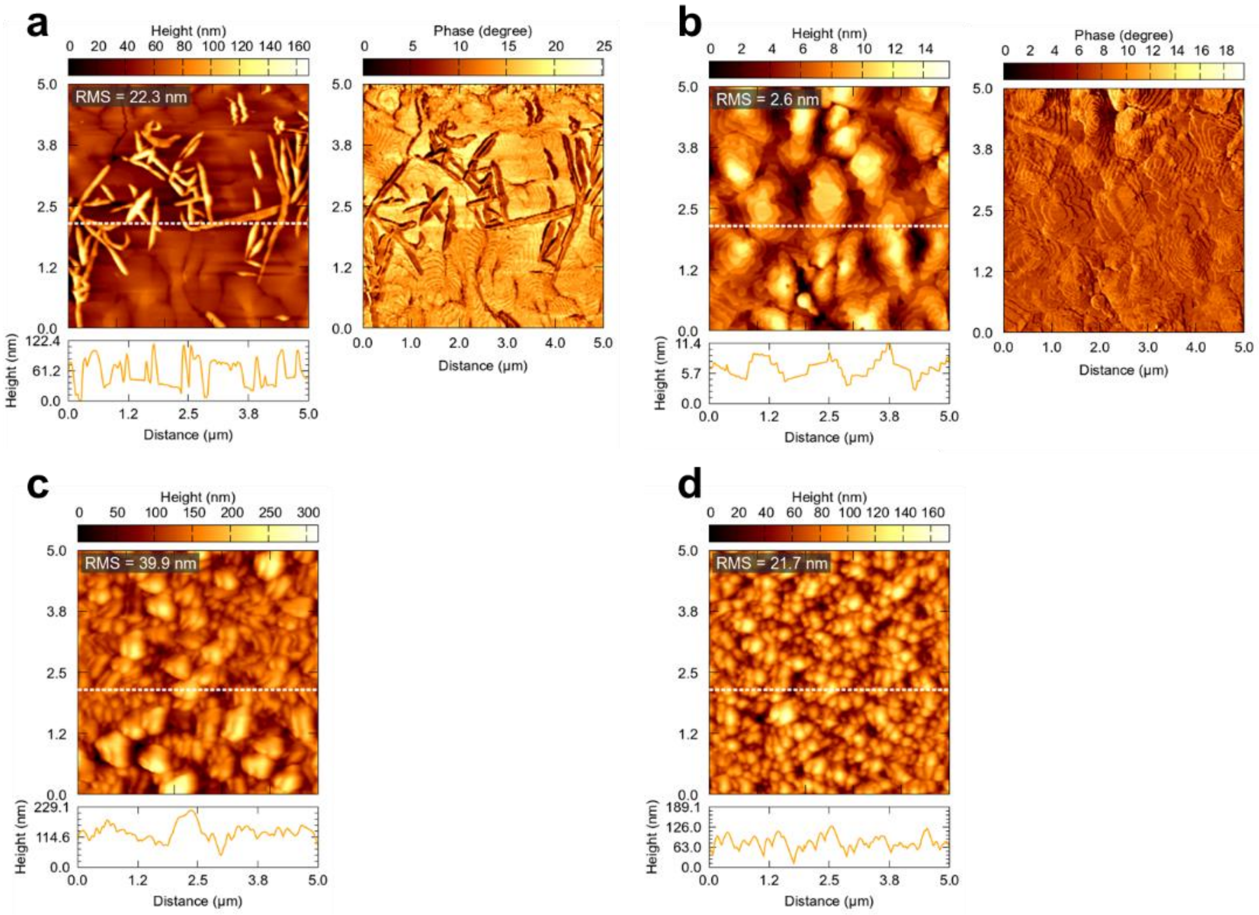

Fig. S7. AFM images of evaporated thin films of Bpin-DNTT (a) and DNTT (b) on bare Si substrate at 100 °C or 60 °C, respectively, and Bpin-DNTT (c) and DNTT (d) on Au substrate at rt. On the bare Si substrates, molecular steps were observed in the phase images for both compounds, indicating that the crystallinity of the thin films is high.

3 Estimation of carrier density

Thin-film transistor: After exposure to ambient air, the source-drain current (I_d) without the gate bias ($V_g = 0$ V) of the Bpin-DNTT-based TFTs was about 10^{-3} A at $V_d = -60$ V, where the channel length (L) and width (W) were 50 and 1500 μm, respectively. Provided that only the surface monolayer (*ca.* 25 Å corresponding to the crystallographic a-axis, d) is air-doped, the relative resistivity (ρ) is calculated as follows:

$$\rho = \frac{V_d}{I_d} \cdot \frac{w \cdot d}{L} = 5.9 \times 10^{-1}\ \Omega\ \mathrm{cm}^{-1}$$

Taking the carrier mobility (μ) of 2.5 $\mathrm{cm}^2\ \mathrm{V}^{-1}\ \mathrm{s}^{-1}$ into account, from the following equation,

$$\sigma = \rho^{-1} = n \cdot \mu \cdot q$$

where n and q are carrier density and elementary charge (1.602×10^{-19} C)

n is calculated to be $4.2 \times 10^{18}\ \mathrm{cm}^{-3}$.

Singel-crystal transistor: Similar to the TFT case, the carrier density (n) in the SC-FETs was estimated. From the transfer characteristics of the SC-FET in Fig. 2e at $V_g = 0$ V, the relative resistivity (ρ) is calculated:

$$\rho = \frac{V_d}{I_d} \cdot \frac{w \cdot d}{L} = 6.0 \times 10^{-1}\ \Omega\ \text{cm}^{-1}$$

where V_d, I_d, w, d, and L are –30 V, 10^{-5} A, 129 µm, 25 Å, and 160 µm, respectively. Similarly, n is calculated to be 3.6×10^{18} cm^{-3}.

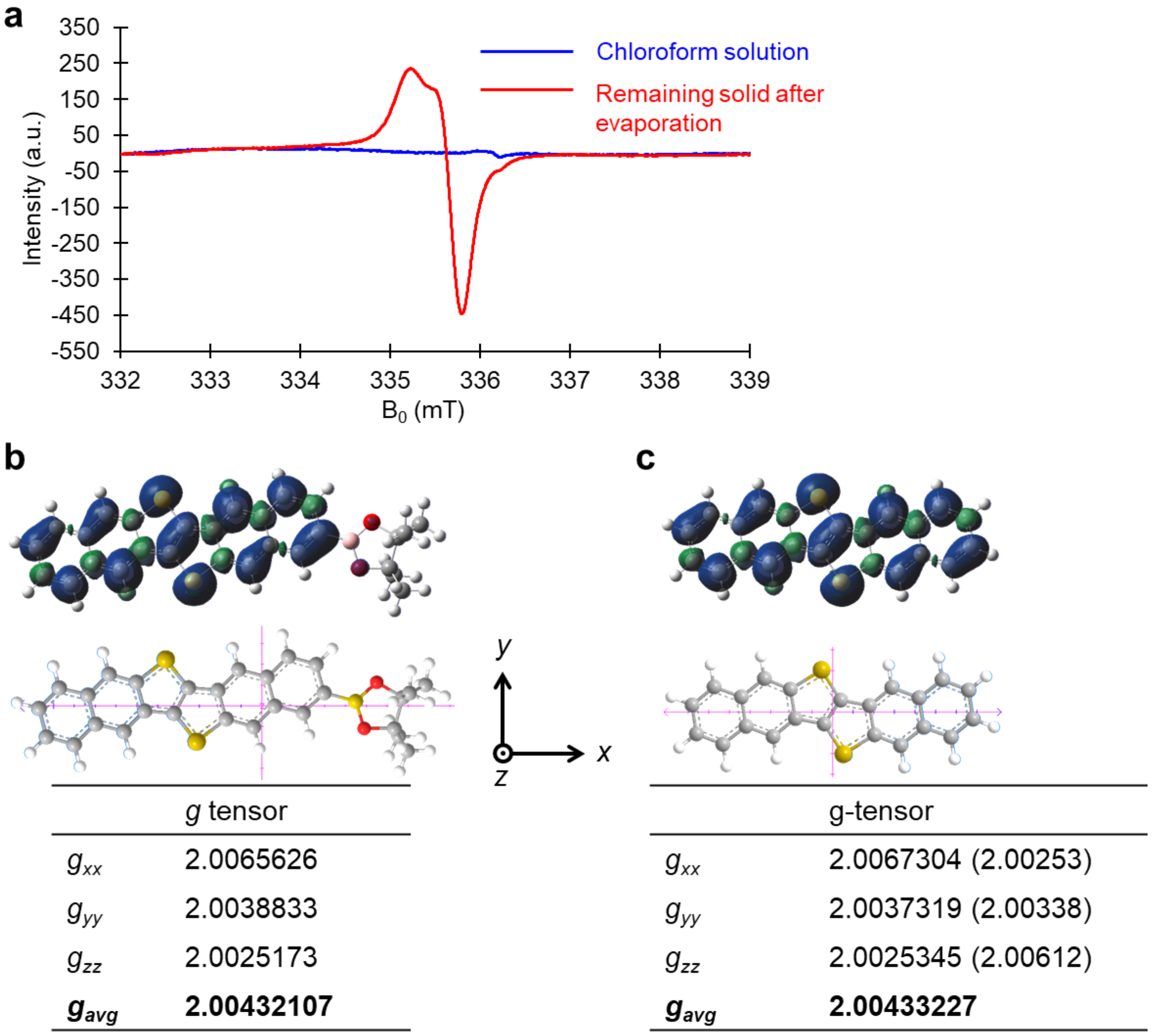

	g tensor
g_{xx}	2.0065626
g_{yy}	2.0038833
g_{zz}	2.0025173
$\mathbf{g_{avg}}$	**2.00432107**

	g-tensor
g_{xx}	2.0067304 (2.00253)
g_{yy}	2.0037319 (2.00338)
g_{zz}	2.0025345 (2.00612)
$\mathbf{g_{avg}}$	**2.00433227**

Fig. S8. (a) ESR spectra of a chloroform solution of Bpin-DNTT (blue trace) and the remaining sample after evaporation. (b) Calculated spin density and *g*-tensor of Bpin-DNTT and (c) DNTT with UB3LYP/6-311G(d,p). For DNTT, the values calculated with UB3LYP/6-311G(d,p) shown in the parentheses are in good accordance with the reported ones. [2]

4 Ultraviolet photoelectron spectroscopy (UPS)

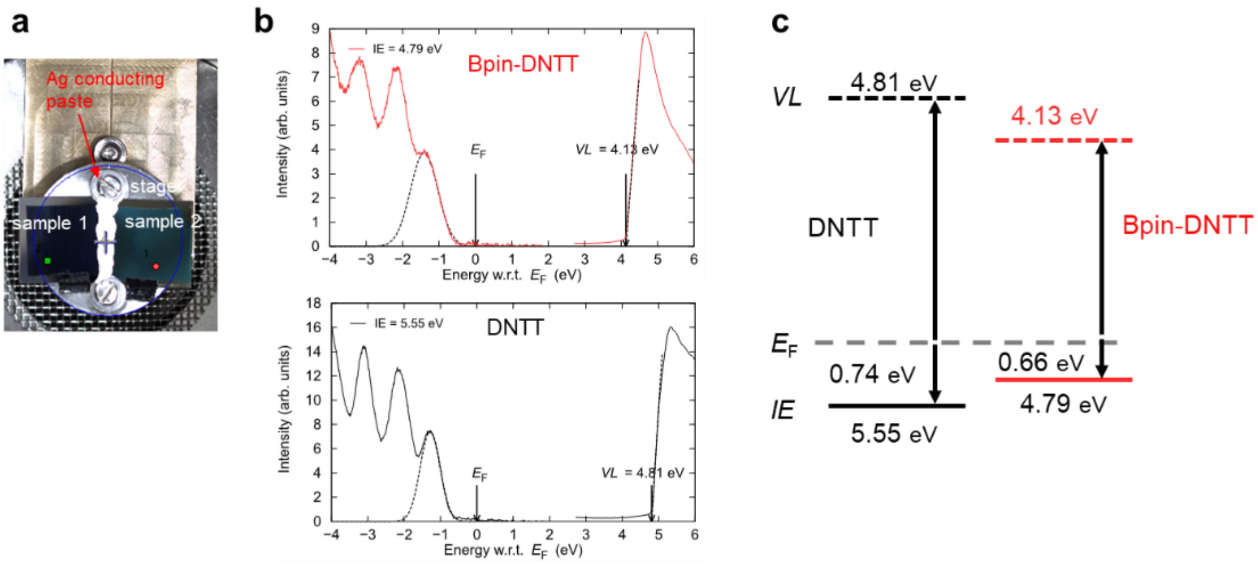

Fig. S9. (a) Sample setup for the UPS measurements, (b) UPS spectra recorded on the Au substrate, and (c) Energy diagrams of Bpin-DNTT and DNTT on the Au substrate.

5 Calculations of intermolecular interaction energies

Intermolecular interaction energies of the Bpin-DNTT face-to-face dimer and various dimeric pairs of DNTT in its crystal structure were calculated by using the SAPT0 methods embedded in the PSI4 program. Table S1 summarizes the data.

Table S1. Intermolecular integration energies for dimers (pairs) in the packing structures of Bpin-DNTT and DNTT calculated by the SAPT method.

Compound	Pair	E_{elect} [a]	E_{exch} [a]	E_{ind} [a]	E_{disp} [a]	E_{SAPT0} [a]
Bpin-DNTT	face-to-face	–11.78	33.20	–3.10	–48.26	–29.94
DNTT[b]	edge-to-face	–6.96	14.71	–1.56	–22.42	–16.22
	edge to-edge	–5.89	9.66	–1.12	–12.71	–10.05
	end-to-end	0.24	0.76	–0.11	–1.72	–0.83

[a] E_{elect}, E_{exch}, E_{ind}, E_{disp}, and E_{SAPT0} are the electrostatic, exchange, induction, dispersion, and the total SAPT0 interaction energy in kcal mol^{-1} calculated with SAPT0/aug-cc-pvdz using the PSI4 program.

[b] The crystal structure was obtained from CCDC-644240.

6 Estimation of difference in electrostatic potential shift (ΔV) due to surface dipole of Bpin-DNTT and DNTT

Based on the Helmholtz equation, the electrostatic potential shifts (ΔV) due to the surface dipole moments can be calculated by

$$\Delta V = \frac{N_{\mathrm{dipole}} \mu_{\mathrm{z}}}{\varepsilon_0 \varepsilon_{norm}} \quad \cdots\cdot (1)$$

where N_{dipole} is the number of surface dipoles per unit area, μ_z is the perpendicular component of the surface dipole moment to the crystallographic *bc* plane (for Bpin-DNTT crystal) or *ab* plane (for DNTT crystal), ε_0 is the vacuum permittivity, and $\varepsilon_{\mathrm{norm}}$ is the relative permittivity of ordinary organic molecules (= 3). On the surface of the *ab*-plane of DNTT crystal and the *bc*-plane of Bpin-DNTT crystal, the local dipole moments of C-H bonds at the 2- or 9-positions and/or C-Bpin fragment should predominantly contribute to the surface dipole moments.

Although it is not easy to determine the local electric dipole moments of fragments of a molecule, the local dipole moment of the C-Bpin moiety in Bpin-DNTT can be roughly estimated to be 2.12 Debye in the direction from the carbon to the boron atom in the C-Bpin fragment. This rough estimation is based on the assumption that the local dipoles in the Bpin-DNTT, except for the C-Bpin fragment at 2-position and the C-H fragment at 9-position (black parts of chemical structures in Fig. S10b), are canceled out similarly to unsubstituted DNTT. This assumption enables the net molecular dipole moment to result from the vector composition between the local dipole moments of the C-Bpin fragment at the 2-position and the C-H fragment at the 9-position. The net molecular dipole moment of Bpin-DNTT with the geometry in the single crystal calculated by the DFT method at the B3LYP/6-311G(d,p) level is 1.72 Debye, which is parallel to the vector from the carbon to boron atoms at the 2-position and is antiparallel to the vector from the carbon to hydrogen atoms at the 9-position. Therefore, the local dipole moment of the C-Bpin fragment should be parallel to the vector from the carbon to the boron atom, with the magnitude of the sum of those of the net dipole moment and the C-H bond dipole moment. Here, the C-H bond dipole was assumed to be 0.40 Debye, thus giving the magnitude of the local dipole moment of the C-Bpin fragment of 2.12 Debye.

Taking into account the tilt angles of these local dipole moments with respect to the crystallographic planes and the areas of the crystallographic planes, the electrostatic potential shifts were estimated from the equation (1) to be 0.20 V for the DNTT crystal and 0.61 V for the Bpin-DNTT crystal, whose difference ($\Delta\Delta V$) is 0.41 V. Note that these estimations took into account of the local dipoles of only C-H and/or C-Bpin fragments at the 2- and 9-positions, but not of those of C-H bonds at the 1-, 3-, 8-, and 10-positions, which should contribute to positive shifts of the electrostatic potential. Thus, the electrostatic potential shifts estimated here might be underestimated, which, however, are to a similar extent for both DNTT and Bpin-DNTT crystals because these C-H fragments are common to both compounds. Therefore, the difference in the electrostatic potential shift ($\Delta\Delta V$) drawn from these estimations should be valid for our purpose of evaluating the effect of the substitution of the Bpin group on the *VL* shift.

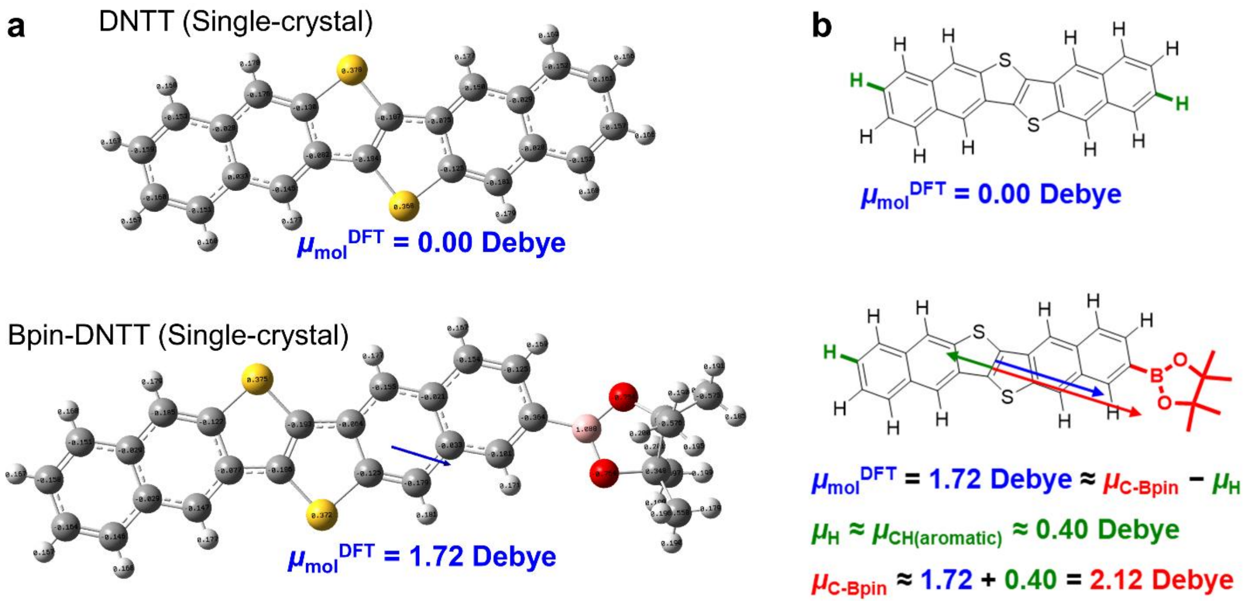

Fig. S10. Molecular dipole moments and atomic charge distributions in DNTT and Bpin-DNTT calculated by natural population analysis (a) and schematic illustration for the estimation of the local dipole moment of the C-Bpin fragment in Bpin-DNTT (b).

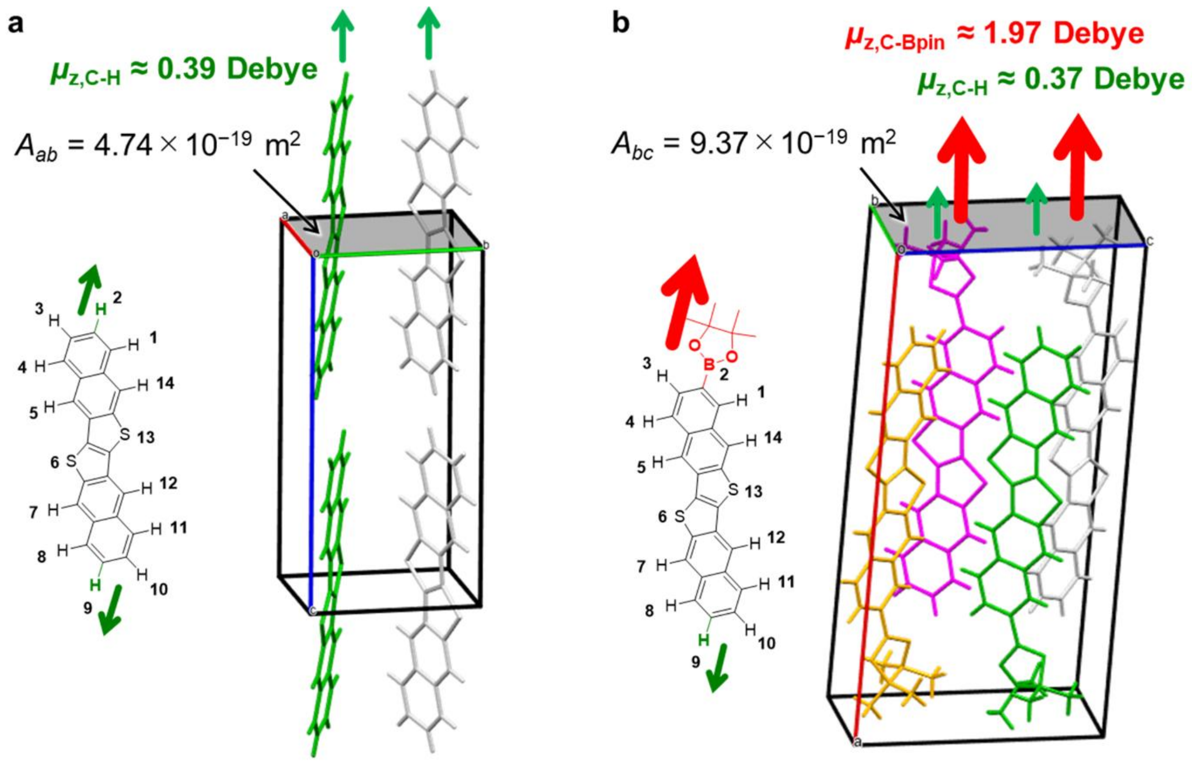

Fig. S11. Schematic illustration for surface dipole moments of the *ab*-plane of DNTT (a) and *bc*-plane of Bpin-DNTT (b), where μ_z is the perpendicular component of the local dipole moments to the planes and A is the area of the crystallographic planes.

7 Evaluation of the effect of polar substituents on electrostatic potential.

To evaluate the effect of the Bpin-group on the electrostatic potential on the crystal surface of Bpin-DNTT, we simulated the electrostatic potential along the normal to the surface of a virtual 2D-monolayer crystal of Bpin-DNTT with periodic boundary conditions along the *b* and *c* axes. The simulations were carried out by the CRYSTAL17 package with the POTC keyword, where the electrostatic potential in the plane at z position (±0.1 Bohr) along the normal to the crystallographic *b*c-plane was averaged. To confirm the effect of the Bpin group in comparison with those of polar C-H and C-F, virtual 2D-monolayer crystals based on dimeric herringbone packing structures of DNTT cores extracted from the Bpin-DNTT crystal structure, which have hydrogen or fluorine atoms at the 2- and/or 9-positions instead of the Bpin group, namely DNTT, F-DNTT, and F2-DNTT, were also simulated. Since the integration of the electrostatic potential over the whole system will be zero because of the neutral system, the potential at infinite ±z will be zero for the symmetric systems in this study. Fig. S12a–d shows the electrostatic potential curve along the z (a*) axis of the virtual 2D-monolayer crystals. Although the shape of potential curves differs depending on the substituents, the shapes of the curves in the range ±7 Å of the crystals (highlighted in pale red color in Fig. S12e) are the same each other because of exactly the same dimeric herringbone packing structures of the DNTT cores. On the other hand, the relative height of the potential curves at the common DNTT part to the infinite vacuum position is different. The averaged potential over the common part in the DNTT crystal is 7.26 V, whereas that in the Bpin-DNTT crystal is 6.46 V, indicating that the vacuum level for the Bpin-DNTT crystal is lower by 0.80 eV than that for the DNTT crystal. This effect was opposite to those observed for fluorinated DNTTs, namely F-DNTT and F2-DNTT, whose vacuum levels are higher by 0.67 and 1.45 eV, respectively, than for the DNTT crystal. Thus, these simulations clearly support that the Bpin group induces a positive shift of the electrostatic potential in the vacuum side, meaning the downward *VL* shift from the DNTT surface.

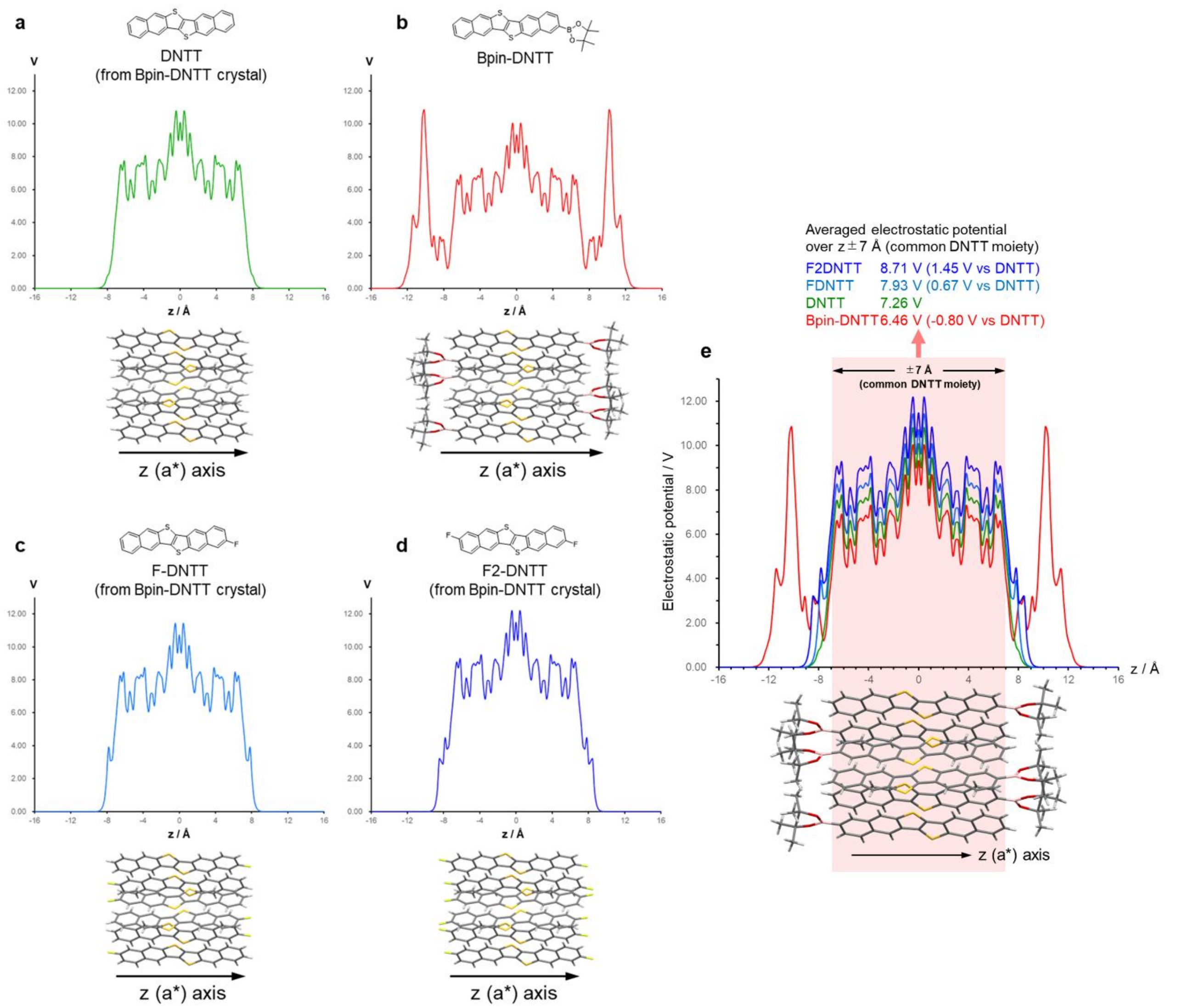

Fig. S12. Simulated electrostatic potential curve along the normal to the virtual 2D-monolayer crystals of substituted DNTT derivatives based on the single crystal structures of Bpin-DNTT (a-d) and overlayed plots with the averaged potentials over ±7 Å along the *z*-axis corresponding to the common DNTT layers.

8 Molecular insights into the strong local dipole in Bpin-DNTT

In sharp contrast to upward *VL* shifts on the OSC surfaces realized mostly by fluorination of the semiconducting core, large downward *VL* shifts have been rarely reported, probably because it is difficult to design a functional group attached to a carbon atom (C-X) that forms a stronger local dipole moment than C-H bonds in the same direction. Hence, it is worth understanding the origin of the large local dipole moment of the C-Bpin fragment. Intuitively, the large local dipole of the C-Bpin fragment seems to result from a highly polarized bond between the carbon atom and the boron atom, which has a lower electronegativity than a hydrogen atom. However, the calculated molecular dipole moments of 2-dihydroborane- or 2-dimethylborane-substituted DNTT, contrary to intuition, point in the opposite direction of that of Bpin-DNTT (Fig. S13 and d), indicating that the polarized C-B bond is not the key structure for the large local dipole in the C-Bpin fragment. Furthermore, removing four methyl groups from the Bpin group does not affect the net molecular dipole moment (Fig. S13e), indicating that the terminal methyl groups are also not the key structure for the large local dipole. On the other hand, with propanediol boronic ester or boronic acid, the net molecular dipoles (3.22 and 2.67 Debye, respectively) were calculated to be larger than that of Bpin-DNTT (Supplementary Figs. 13f and 13g). The structure-dipole relationships and charge distribution by natural population analysis suggest that the large dipoles from C to B direction (parallel to the x-axis in Fig. S13f) of these boronic esters and boronic acid originate from the pair of symmetric B-O-C or B-O-H substructures, where the large bond dipoles of the two highly polar B-O bonds are largely canceled out each other in a perpendicular direction to the x-axis (black vector components) with a small residual bond dipole (green vector components) antiparallel to the x-axis while the large bond dipole of the two O-C or O-H bonds mostly points parallel to the x-axis resulting in the large local dipole moments parallel to the x-axis.

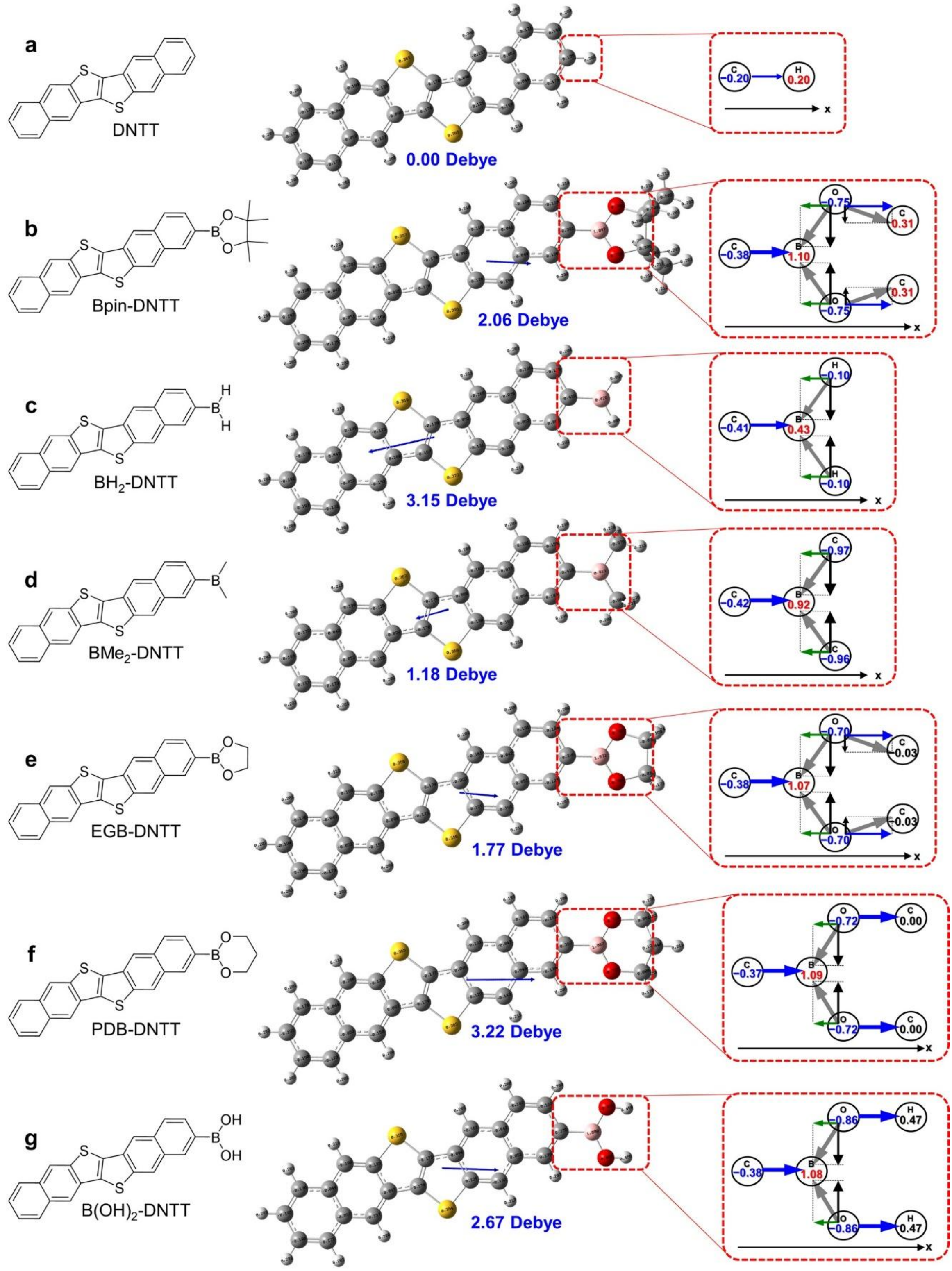

Fig. S13. Charge distribution by natural population analysis and molecular dipole moments of DNTT and its boron-substituted derivatives with the optimized geometry by the DFT method, and schematic illustrations of the local bond dipole at the 2-position. Blue and green arrows in the red frames represent the vector components in parallel and antiparallel, respectively, to the x-axis, which is along the C-to-B (H) direction at the 2-position. Black arrows represent the vector components perpendicular to the x-axis, which are canceled out.

9 Electronic structures of molecular clusters

The electronic structures of single-molecule molecular clusters with geometries extracted from the single crystal structures of DNTT and Bpin-DNTT were calculated by using the CRYSTAL17 package with the MOLECULE command at the level of B3LYP/631G(d,p).

The HOMO and LUMO energy levels of the single molecule of DNTT and Bpin-DNTT are split into a wide range of energy levels as the number of molecules in the cluster increases (Fig. S14 and Fig. S15). As a result, the HOMO energy level of monomer (−5.03 eV) was split into eight different energy levels in the 8mer cluster, which range over 0.50 eV form HOMO−7 at −5.11 eV to HOMO at −4.61 eV. In the Bpin-DNTT clusters, the HOMO energy level of monomer (−4.96 eV) was split into eight different energy levels in the 8mer cluster, which range over 0.57 eV from HOMO−7 at −4.85 eV to HOMO at −4.28 eV. Remarkably, the shift of the HOMO energy levels from the monomer to 8mer of Bpin-DNTT (0.68 eV) is much larger than that of DNTT (0.42 eV), which is consistent with the band calculation results. It should be noted that among the 2mer clusters of Bpin-DNTT, the face-to-face π-stacking 2mer cluster (2-pi) has significantly higher HOMO energy levels than those of the other two 2mer clusters, clearly indicating that the strong anti-parallel face-to-face dimerization in the Bpin-DNTT contributes to the significant upward shift of the HOMO band edge in the crystal.

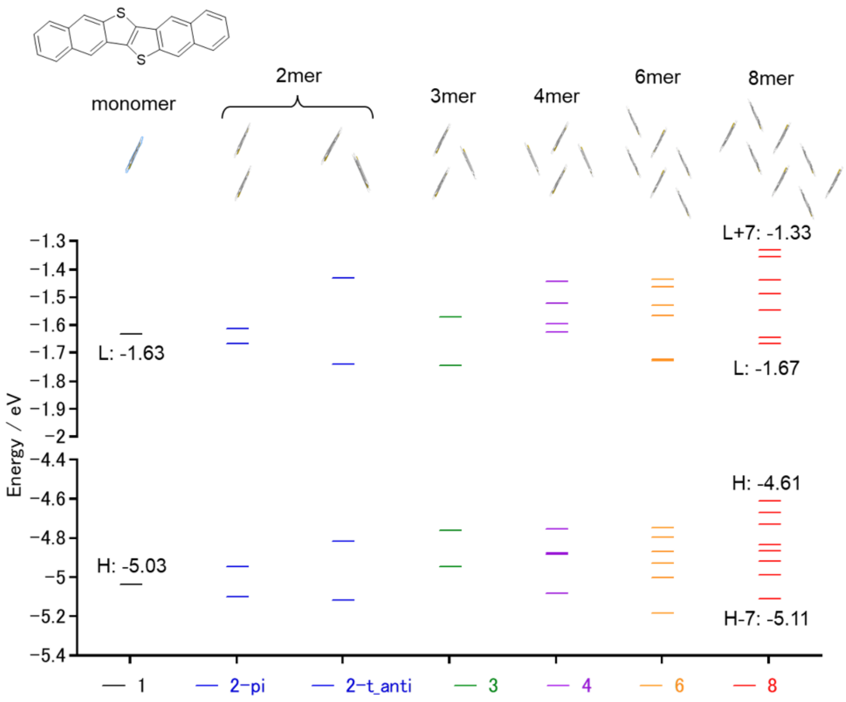

Fig. S14. Diagrams of orbital energy levels of molecular clusters of DNTT.

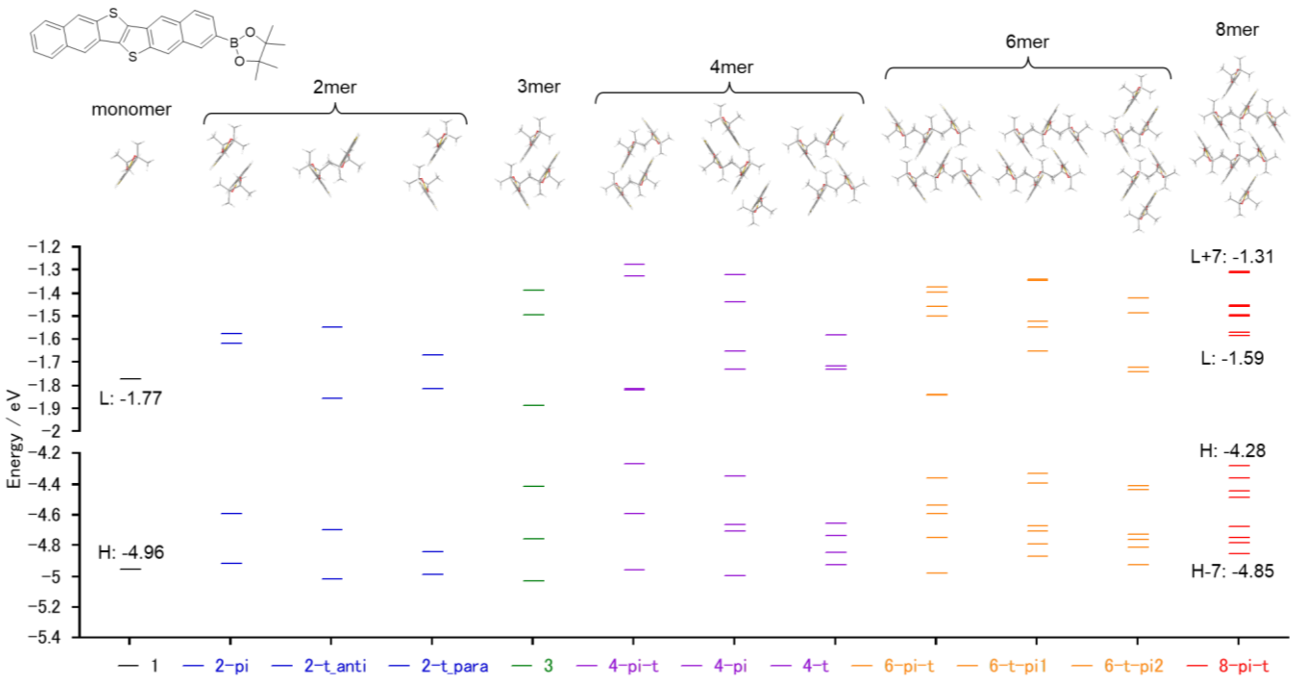

Fig. S15. Diagrams of orbital energy levels of molecular clusters of Bpin-DNTT.

10 Bpin-modified [1]benzothieno[3,2-*b*]naphtho[2,3-*b*]thiophene (Bpin-BTNT)

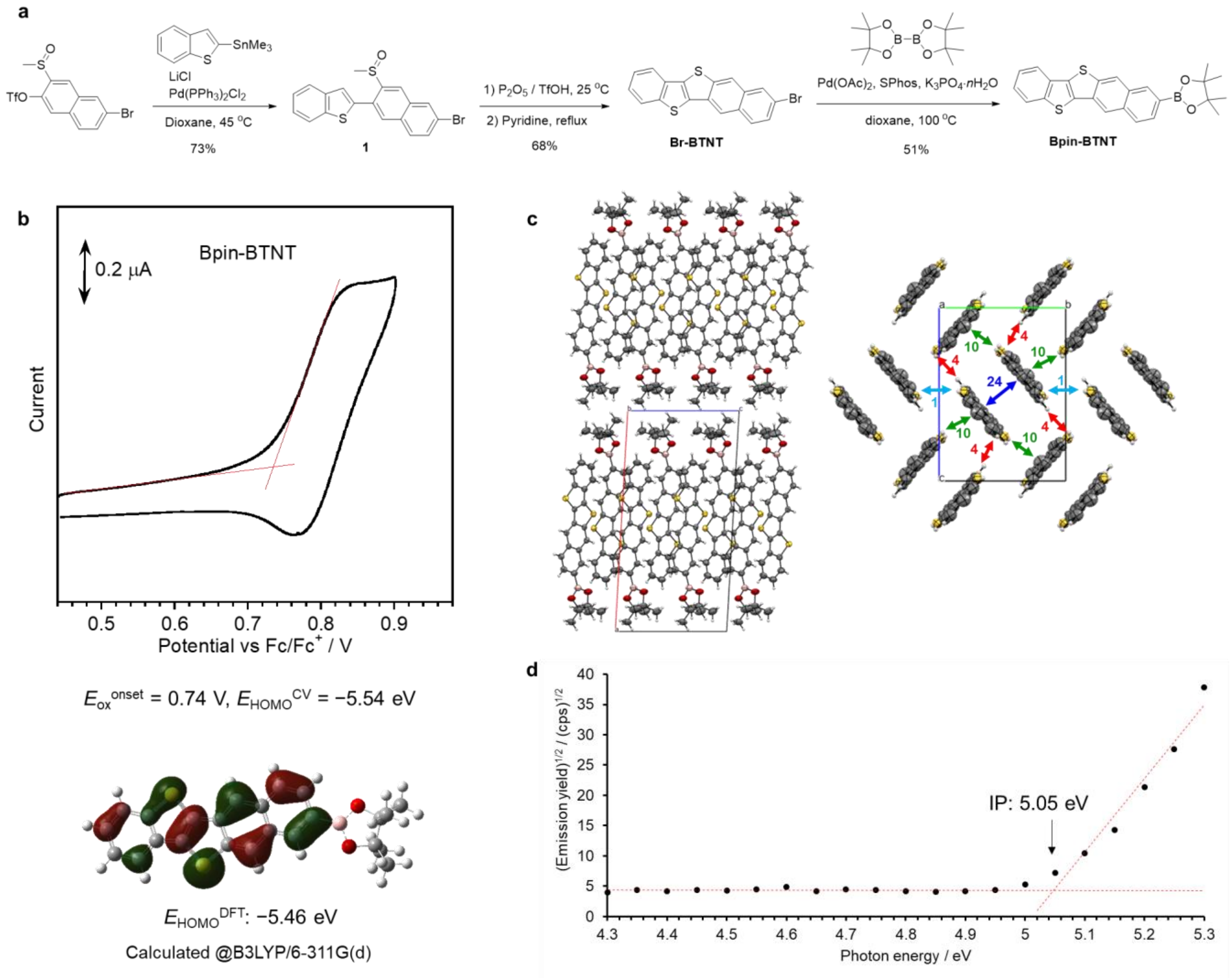

Fig. S16. (a) Synthesis of Bpin-BTNT. (b) CV and thus estimated E_{HOMO} of Bpin-BTNT, together with the calculated HOMO of Bpin-BTNT. (c) Crystal structure of Bpin-BTNT with calculated intermolecular electronic couplings of HOMOs (meV). Crystal data: yellow plate, *monoclinic*, $P2_1$/c, $a = 22.4468(4)$, $b = 8.2690(1)$, $c = 11.3256(2)$ Å, $b = 93.235(2)°$, $V = 2098.82(6)$ Å^3, $Z = 4$, $T = 293(2)$ K, $R = 0.0337(3821)$, $wR^2 = 0.0998(4195)$, GOF = 1.073 (CCDC-2519941). (d) IP of Bpin-BTNT evaluated by photoemission yield spectroscopy in air (PYSA).

Synthesis of 2-(6-bromo-3-(methylsulfinyl)naphthalen-2-yl)benzo[*b*]thiophene (1)

A solution of 6-bromo-3-(methysulfinyl)naphthalen-2-yl trifluoromethanesulfonate (4.17 g, 10.0 mmol), benzo[*b*]thiophen-2-yltrimethylstannane (3.09 g, 10.4 mmol), lithium chloride (1,27 g, 30.0 mmol), and tetrakis(triphenylphosphine)palladium(II)dichloride (0.14 g, 0.20 mmol) in 1,4-dioxane (125 mL) was stirred at 45 °C for 48 h. Then, the reaction mixture was quenched with water (300 mL) and extracted with DCM (400 mL). The extract was washed with water (200 mL) and dried over magnesium sulfate. The crude product was purified by silica gel column chromatography (eluent: dichloromethane), giving **1** as a white solid (2.93 g, 73.1 mmol, 73%). mp. 183.5−184.6 °C. ^{1}H NMR ($CDCl_3$, 500 MHz): δ (ppm) 8.19 (d, $J = 1.5$ Hz, 1H), 7.99 (s, 1H), 7.89 (d, $J = 7.5$ Hz, 1H), 7.85 (dd, $J = 7.0, 1.5$ Hz, 1H), 7.80 (d, $J = 8.5$ Hz, 1H), 7.70 (dd, $J = 8.8, 1.8$ Hz, 1H), 7.52 (s, 1H), 7.46−7.40

(m, 2H), 2.52 (s, 3H). ^{13}C NMR ($CDCl_3$, 100 MHz): δ (ppm) 143.63, 140.26, 139.93, 138.47, 133.82, 132.29, 131.73, 130.82, 130.54, 129.56, 128.59, 125.23, 125.05, 124.56, 124.20, 123.85, 122.25, 121.98, 42.10. HRMS (EI) *m/z*: Calcd. for $C_{19}H_{13}BrOS_2$ $[M]^+$: 399.9586. Found: 399.9599.

Synthesis of 8-bromobenzo[4,5]thieno[3,2-*b*]naphtho[2,3-*d*]thiophene (Br-BTNT)

To a mixture of **1** (200 mg, 0.50 mmol) and phosphorous pentoxide (106 mg, 0.75 mmol), was added trifluoromethane sulfonic acid (5.0 mL). The mixture was stirred at 25 °C for 3 days, then poured into ice water (40 mL). The pale yellow precipitates were collected by filtration and dried in vacuo. The resulting solid was suspended in pyridine (20 mL), and the mixture was refluxed for 2 hours. The mixture was poured into methanol (100 mL), and the pale yellow precipitates were collected by filtration and further purified by silica gel column chromatography (eluent: chloroform) to give Br-DNTT as a pale yellow solid (126 mg, 0.34 mmol, 68%). mp. 323.2−324.5 °C. ^{1}H NMR ($CDCl_3$, 500 MHz): δ (ppm) 8.32 (s, 1H), 8.30 (s, 1H), 8.10 (s, 1H), 7.96 (d, J = 7.5 Hz, 1H), 7.91−7.88 (m, 2H), 7.57 (dd, J = 9.0, 1.5 Hz, 1H), 7.51−7.44 (m, 2H). ^{13}C NMR ($CDCl_3$, 101 MHz): δ (ppm) 142.93, 141.97, 135.00, 133.29, 132.77, 132.68, 132.21, 129.82, 129.70, 129.29, 129.13, 125.60, 125.19, 124.16, 122.05, 121.52, 119.76, (one carbon signal could be overlapped). HRMS (EI) *m/z*: Calcd. for $C_{18}H_9BrS_2$ $[M]^+$: 367.9324. Found: 367.9322. Anal. Calcd. for $C_{18}H_9BrS_2$: C, 58.54; H, 2.46%. Found: C, 58.48; H, 2.52%.

Synthesis of 2-(benzo[4,5]thieno[3,2-*b*]naphtho[2,3-*d*]thiophen-8-yl)-4,4,5,5-tetramethyl-1,3,2-dioxaborolane (Bpin-BTNT)

4,4,4',4',5,5,5',5'-Octamethyl-2,2'-bi(1,3,2-dioxaborolane) (550 mg, 2.17 mmol), Br-BTNT (80 mg, 0.22 mmol), SPhos (4.5 mg, 0.011 mmol), tri-potassium phosphate *n*-hydrate (139 mg, 0.65 mmol), and palladium acetate (1.0 mg, 0.0045 mmol) were added to a Schlenk tube. The Schlenk tube was evacuated, backfilled with argon, and then filled with nitrogen. Distilled 1,4-dioxane (6 mL) was added via syringe. The reaction mixture was heated at 100 °C for 20 hours. After the reaction mixture was allowed to cool to room temperature, the mixture was filtered by chromatography on silica-gel (solvent: chloroform), The residue was collected by filtration and washed with MeOH, purified by gel permeation chromatography (eluent: chloroform) and further purified by vacuum sublimation (source temperature 170-210 °C under 10^{-3} Pa) to give Bpin-BTNT as yellow powder (46 mg, 0.11 mmol, 51%). mp 266.5–267.6 °C. ^{1}H NMR ($CDCl_3$, 500 MHz): δ (ppm) 8.45 (s, 1H), 8.39 (s, 1H), 8.30 (s, 1H), 7.97 (d, J = 8.0 Hz, 1H), 7.92 (d, J = 7.5 Hz, 1H), 7.88−7.85 (m, 2H), 7.46 (t, J = 7.3 Hz, 1H), 7.41 (t, J = 7.5 Hz, 1H), 1.41 (s, 12H). ^{13}C-NMR ($CDCl_3$, 101 MHz): δ (ppm) 142.77, 140.46, 135.86, 134.99, 133.17, 133.10, 132.69, 132.55, 130.60, 129.94, 127.23, 125.44, 125.03, 124.09. 123.29, 122.00, 119.53, 84.03, 24.95, (A signal from the *ipso*-carbon atom to the pinacolborane group was too weak to be observed, probably due to the quadrupole moments of the boron nuclei). HRMS (APCI) *m/z*: Calcd. for $C_{24}H_{21}BO_2S_2$ $[M]^+$: 416.1071. Found: 416.1067.

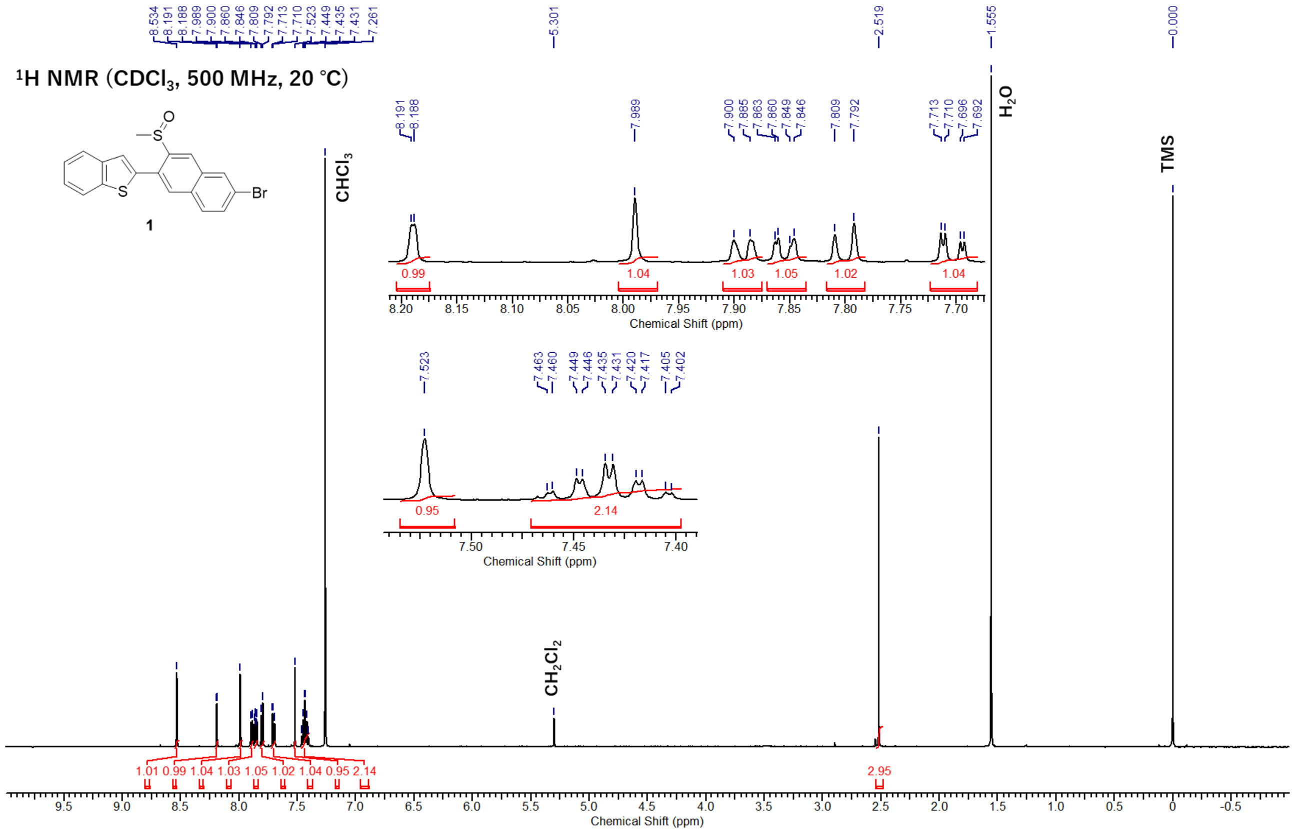

Fig. S17. ¹H NMR spectrum of **1**.

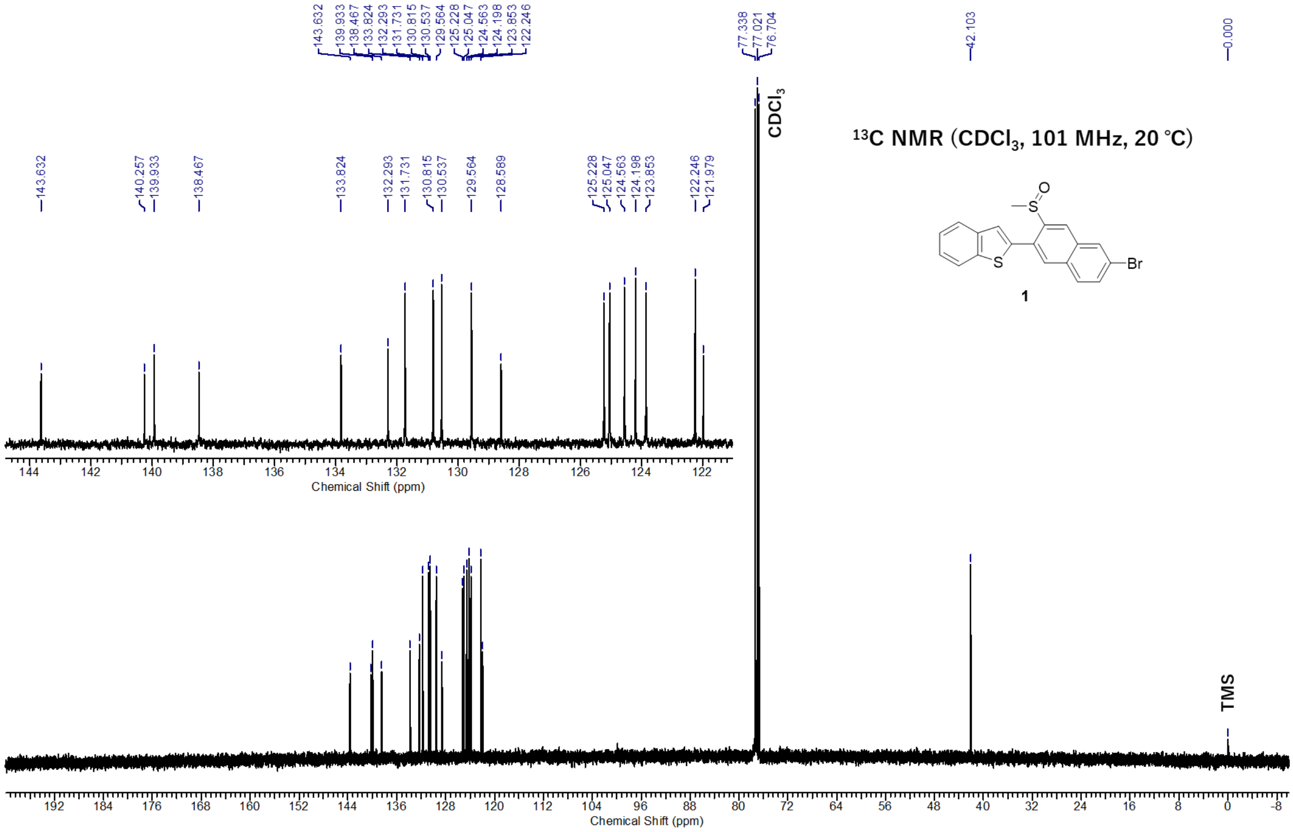

Fig. S18. ¹³C NMR spectrum of **1**.

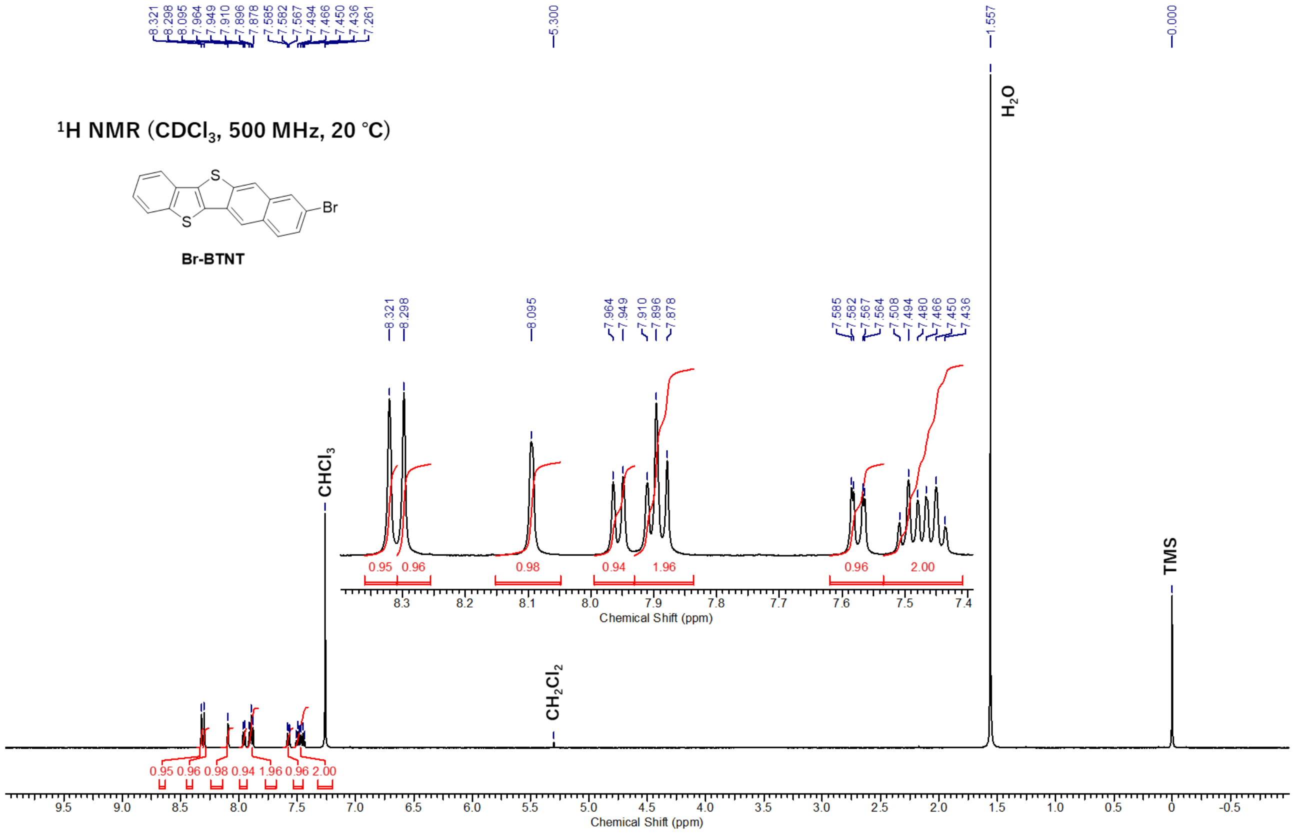

Fig. S19. ^{1}H NMR spectrum of Br-BTNT.

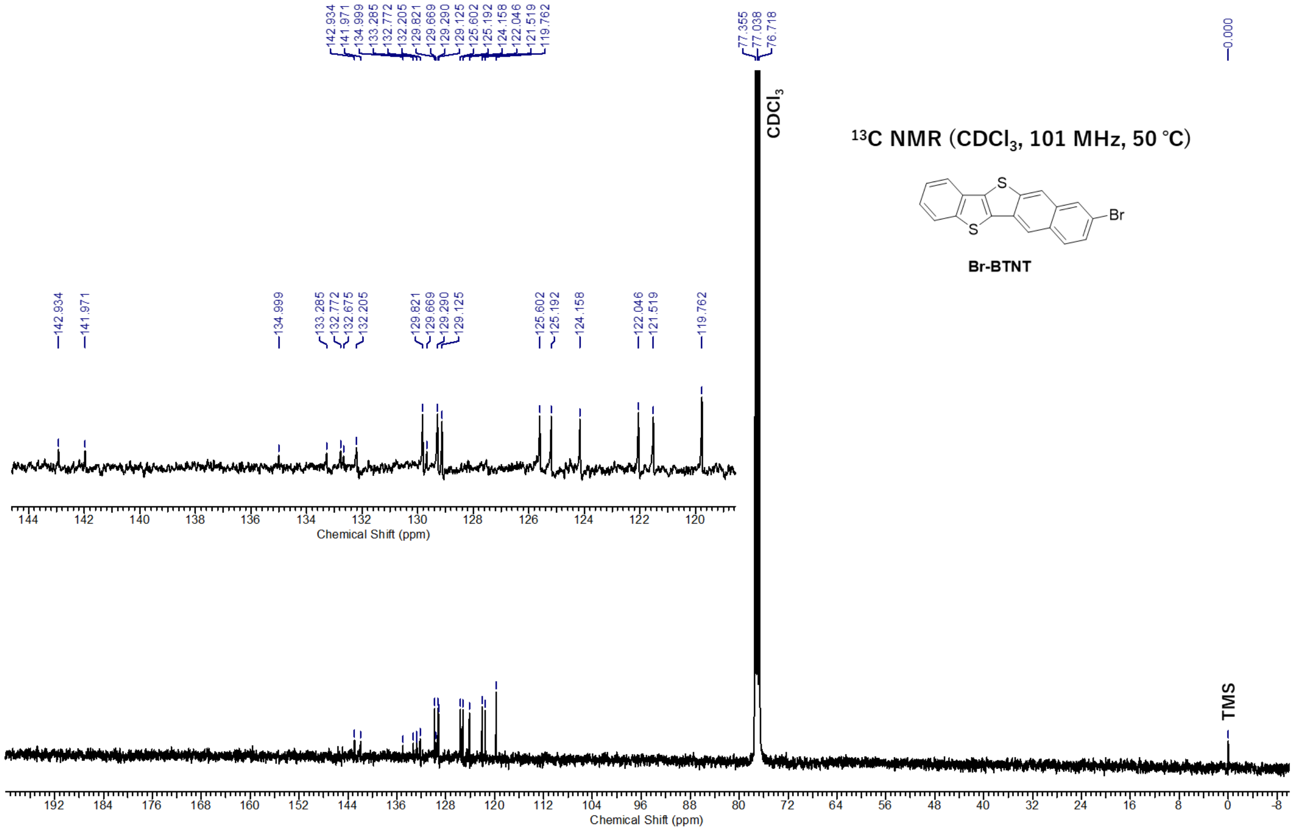

Fig. S20. ^{13}C NMR spectrum of Br-BTNT.

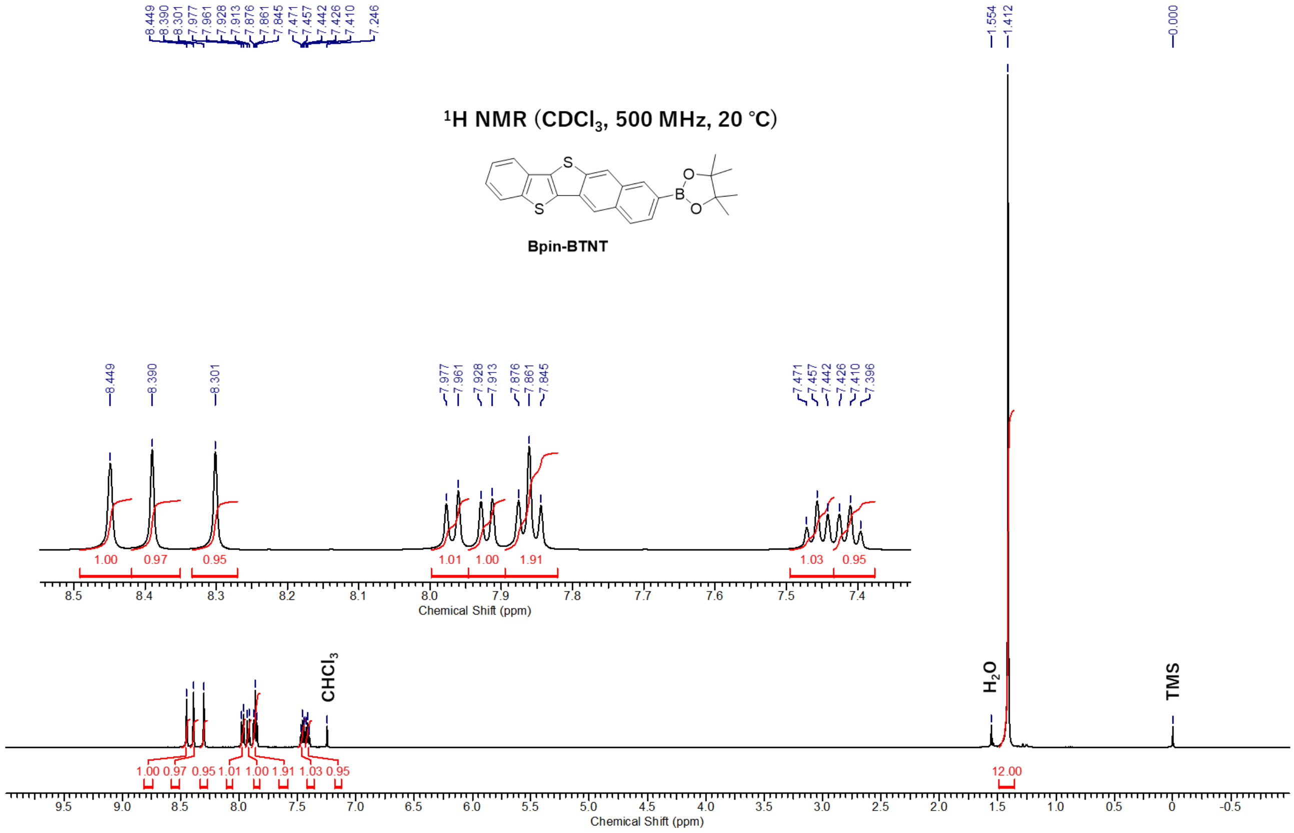

Fig. S21. ^{1}H NMR spectrum of Bpin-BTNT.

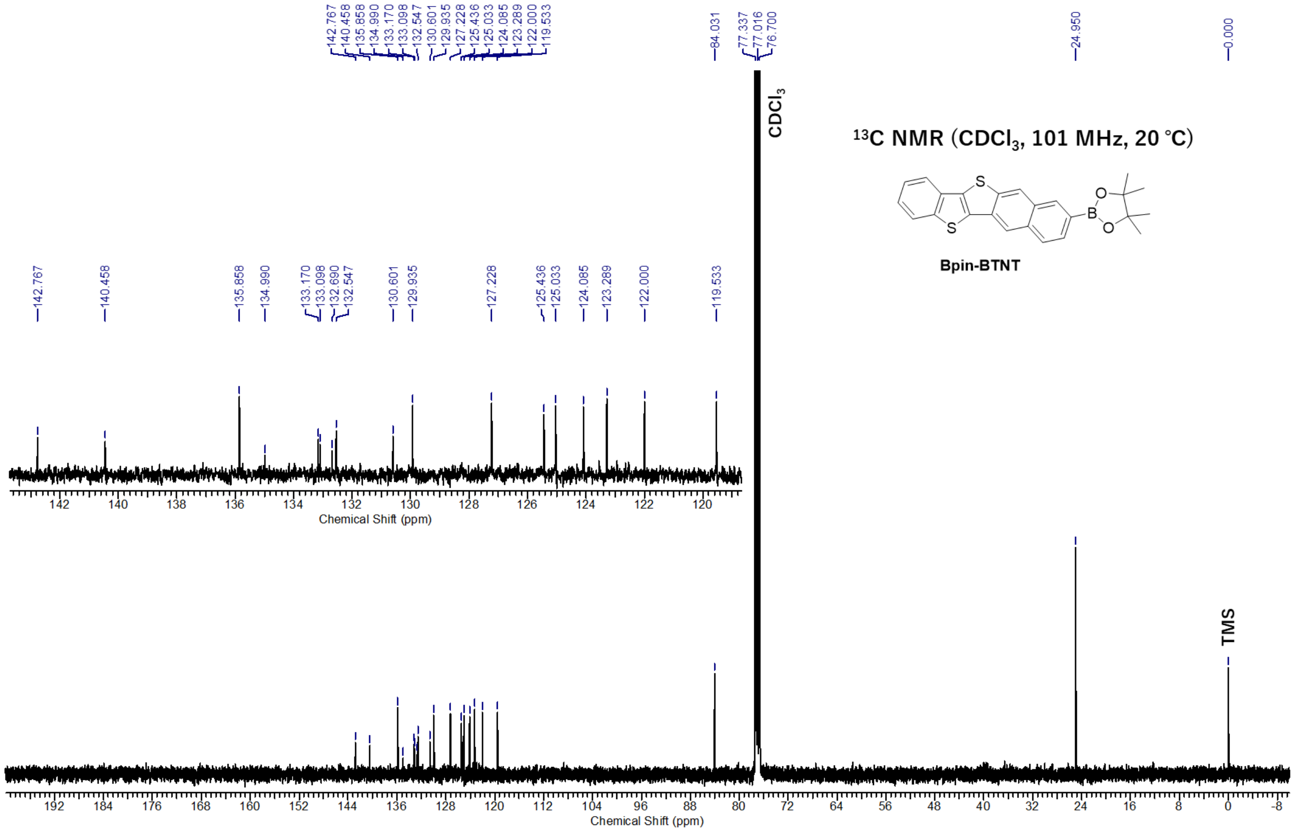

Fig. S22. ^{13}C NMR spectrum of Bpin-BTNT.

11 References

1. M. J. Frisch, G. W. Trucks, H. B. Schlegel, G. E. Scuseria, M. A. Robb, J. R. Cheeseman, G. Scalmani, V. Barone, G. A. Petersson, H. Nakatsuji, X. Li, M. Caricato, A. V. Marenich, J. Bloino, B. G. Janesko, R. Gomperts, B. Mennucci, H. P. Hratchian, J. V. Ortiz, A. F. Izmaylov, J. L. Sonnenberg, D. Williams-Young, F. Ding, F. Lipparini, F. Egidi, J. Goings, B. Peng, A. Petrone, T. Henderson, D. Ranasinghe, V. G. Zakrzewski, J. Gao, N. Rega, G. Zheng, W. Liang, M. Hada, M. Ehara, K. Toyota, R. Fukuda, J. Hasegawa, M. Ishida, T. Nakajima, Y. Honda, O. Kitao, H. Nakai, T. Vreven, K. Throssell, J. A. Montgomery Jr., J. E. Peralta, F. Ogliaro, M. J. Bearpark, J. J. Heyd, E. N. Brothers, K. N. Kudin, V. N. Staroverov, T. A. Keith, R. Kobayashi, J. Normand, K. Raghavachari, A. P. Rendell, J. C. Burant, S. S. Iyengar, J. Tomasi, M. Cossi, J. M. Millam, M. Klene, C. Adamo, R. Cammi, J. W. Ochterski, R. L. Martin, K. Morokuma, O. Farkas, J. B. Foresman and D. J. Fox, Gaussian 16 Rev. C.01, 2016.
2. H. Matsui, D. Kumaki, E. Takahashi, K. Takimiya, S. Tokito and T. Hasegawa, Correlation between interdomain carrier hopping and apparent mobility in polycrystalline organic transistors as investigated by electron spin resonance, *Phys. Rev. B*, 2012, **85**, 035308.